

Application of fast factorized back-projection algorithm for high-resolution highly squinted airborne SAR imaging

Lei ZHANG^{1,2*}, Haolin LI^{1,3}, Zhiwei XU^{1,2} & Hongxian WANG^{1,2}

¹National Laboratory of Radar Signal Processing, Xidian University, Xi'an 710071, China;

²Collaborative Innovation Center of Information Sensing and Understanding, Xidian University, Xi'an 710071, China;

³Beijing Institute of Electronic System Engineering, Beijing 100854, China

Received May 25, 2016; accepted July 29, 2016; published online December 13, 2016

Abstract In squinted synthetic aperture radar (SAR) imaging, the range-azimuth coupling requires precise range cell migration correction (RCMC). Moreover, for high-resolution airborne SAR, motion compensation (MOCO) becomes complicated as the squint angle increases, thereby degrading the performance of Doppler-domain imaging algorithms. On the other hand, time-domain back-projection (BP) SAR imaging approaches are considered as optimal solutions to performing precise image focusing and MOCO. Among current BP algorithms, the fast factorized back-projection (FFBP) algorithm is one of the most essential representatives that achieve high-resolution images in an efficient manner. In this paper, the principle and applications of the FFBP algorithm are investigated through the derivation of the azimuth impulse response function (AIRF) of the resulting image. The phenomenon of spectrum displacement induced by motion errors in the BP image is presented and analyzed. Based on rigorous mathematical derivations, a modified FFBP algorithm is proposed to facilitate a seamless integration with motion compensation and accurate imagery of high-resolution highly squinted airborne SAR. Real data results confirm the effectiveness of the proposed approaches.

Keywords synthetic aperture radar (SAR), fast factorized back-projection (FFBP), modified fast factorized back-projection (MFFBP), squinted SAR, motion compensation (MOCO)

Citation Zhang L, Li H L, Xu Z W, et al. Application of fast factorized back-projection algorithm for high-resolution highly squinted airborne SAR imaging. *Sci China Inf Sci*, 2017, 60(6): 062301, doi: 10.1007/s11432-015-0927-3

1 Introduction

Synthetic aperture radar (SAR) is a well-established powerful microwave remote sensing technique that enables high-resolution observation in both range and azimuth directions. The high range and azimuth resolutions are determined by the bandwidth of the transmitted signal and the size of the synthetic aperture, respectively. SAR has been a capable and effective means for the retrieval of geographical information. In a SAR configuration, the angle between the pointing direction of the antenna beam center and the direction perpendicular to the flight path is defined as the squint angle [1, 2]. SAR systems

* Corresponding author (email: leizhang@xidian.edu.cn)

can be operated in different modes depending on how the antenna beams scan the scene. Among them, squint mode is an important one which not only increases the flexibility of trajectory design, but also equips the SAR system with the forward-looking ability. However, precisely focusing of squinted SAR data is a difficult task due to the fact that the coupling between range and azimuth is much more significant than that in the broadside mode. As such, the precision of range cell migration correction (RCMC) is compromised when using conventional SAR algorithms. The range-azimuth coupling can be resolved, or at least substantially reduced, by Doppler-domain RCMC processing, which includes scaling using the chirp-scaling algorithms (CSAs) [3–10] and the Stolt mapping using the Omega-k algorithms [11–14]. Note that all these methods utilize the “azimuth-shift-invariance” property of the ideal SAR transfer function and perform RCMC in the Doppler domain. We refer to them as the Doppler-domain algorithms. In handling squinted SAR data, precise RCMC becomes difficult for the Doppler-domain algorithms as the range-azimuth coupling becomes more significant.

In addition to the coupling effects, motion compensation (MOCO) is another crucial issue for high-resolution airborne squinted SAR imaging. Motion errors are inevitable due to the atmospheric turbulence and platform vibration, especially when small-size unmanned aerial vehicle (UAV) SAR platforms are considered. In general, MOCO mainly relies on the high-accuracy measurements of the trajectory deviations by the mounted position system (POS). One of the important MOCO approaches is the “two-step” method [5,14]. In this method, the spatial-invariant part of the motion error is corrected in the raw data, where as the RCMC is performed in the Doppler domain and is then followed by the correction of the range-dependent part. The “two-step” MOCO is based on the center-beam assumption [15], it works well in the broadside SAR or when the squint angle is small. Some novel topography- and aperture-dependent MOCO algorithms [16–19] have been developed recently to handle the residual phase errors after the “two-step” MOCO and, subsequently, achieve enhanced focusing performance. However, those MOCO approaches are not directly applicable to highly squinted airborne SAR when the motion error is large. In this case, the spatial variance of motion error becomes significant [20] and, therefore, Doppler-domain RCMC processing algorithms become very sensitive and fragile to motion errors. It has been revealed in [21] that, in highly squinted SAR imaging, direct application of Doppler-domain RCMC algorithms may not be tolerable to even a very small motion error. It was also pointed out in [22] that a small motion error would yield a crucial influence on RCMC in the polar formation algorithm (PFA). In order to handle the azimuth-dependent terms in focusing high-squint SAR data with motion errors, advanced strategies, like azimuth frequency subaperture processing [23], are necessary to reduce the problem in range-azimuth de-coupling and motion compensation. It is clear from the above discussion that conventional MOCO approaches that incorporate Doppler-domain imaging algorithms may not work in high-resolution imaging for squinted airborne SAR, especially in the presence of severe motion errors. Those difficulties in both precise RCMC and MOCO for high-resolution highly squinted airborne SAR imaging motivate our work in this paper.

On the other hand, time-domain back-projection (BP) algorithms have been investigated as a promising alternative for SAR imaging [24]. Rooted in the basic principle of wideband beam-forming, the BP algorithm, in theory, offers a number of advantages over the Doppler-domain counterparts, such as its capability of precisely compensating the curved wave-front effects for arbitrary SAR configurations, and optimal compatibility of topography- and aperture-dependent MOCO [25,26]. Different from the Doppler-domain algorithms that first transform the data into the Doppler domain, BP distinguishes itself by performing the BP integral directly in the time domain. As such, the trajectory deviations can be precisely accounted for by utilizing the measured POS information. Despite of these advantages, the direct application of BP often finds difficult in practice due to its low efficiency because the point-to-point integral is highly time-consuming. Great efforts have been devoted to accelerate the BP processing by developing fast BP (FBP) algorithms [27–31]. These algorithms achieve a higher efficiency while inheriting the advantages of the original BP algorithm. Among them, the fast factorized back-projection (FFBP) algorithm [30] is one of the most useful techniques which divide a long synthetic aperture into a series of short sub-apertures (SAs), each being focused in the BP integral to generate an SA image with a coarse angular resolution. These coarse images are then recursively fused to yield a high-resolution

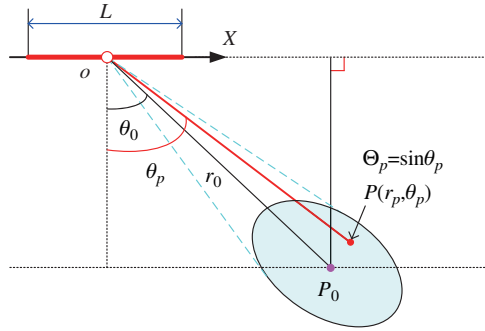


Figure 1 (Color online) Squinted SAR geometry.

SAR image. The FFBP is of prominent potential in focusing high-resolution SAR data due to its high precision, while its efficiency is close to that of the conventional Doppler-domain algorithms [32].

The high precision and efficiency of the FFBP make it a desirable solution to different SAR formations. Nevertheless, as we will see later in this paper, direct application of the FFBP still encounters challenges in dealing with highly squinted SAR data when the motion errors are severe. In particular, the FFBP may fail in the SA fusion stages if the spectrum displacements in the SA BP images due to the motion errors are not properly accounted for. This fact motivates us to develop the modified FFBP for improved airborne highly squinted SAR imagery. Our main contributions can be specified as follows. The applicability of the FFBP algorithm for squinted airborne SAR imaging is investigated, and significant modifications are proposed to make the SA fusion applicable to severe motion compensation. It is revealed that, in the standard FFBP formation for highly squinted SAR imaging, severe motion errors easily induce a special spectrum displacement in the SA images even after they are compensated in the SA BP integral. The spectrum displacement should be carefully accounted for to ensure the success of SA fusion within the SA fusion recursion. Real measured data with severe trajectory deviations are used to show the validity of the modification to FFBP application on focusing highly squinted SAR data.

This paper is organized as follows. Section 2 reviews the signal model of an airborne squinted SAR and the principle of the FFBP algorithm. The application of FFBP in the airborne squinted SAR data processing is addressed in Section 3. The combined use of accurate MOCO and FFBP is presented, and the specific issue of spectrum shift is analyzed in detail. Section 4 provides processed results for real-data experiments. Finally, Section 5 concludes this paper.

2 Squinted SAR signal model and BP algorithms

2.1 Squinted SAR signal model

Figure 1 shows an ideal geometry of a squinted SAR. In this figure, the SAR sensor travels along the x axis with a constant velocity v . Referring the aperture center as the coordinate origin, the polar coordinate of the scene center P_0 can be defined as (r_0, θ_0) , where θ_0 is the center squint angle. Consider an arbitrary point target P , located at (r_p, θ_p) , with a unit scattering amplitude. For the convenience of the introduction of the BP integral, we define $\Theta_p = \sin \theta_p$. Similarly, we also define $\Theta_0 = \sin \theta_0$ and $\Phi_0 = \cos \theta_0$. During the data acquisition, the slant range between the radar and the target P is given by

$$R(r_p, \Theta_p; X) = \sqrt{r_p^2 + X^2 - 2r_p X \Theta_p}, \quad -\frac{L}{2} < X \leq \frac{L}{2}, \quad (1)$$

where X is the instantaneous position of the radar, whereas the corresponding time delay is $t_p = 2R(r_p, \Theta_p; X)/c$, and c is the propagation velocity of light. Assume that a linear frequency modulated (LFM) signal with pulse width T_p and chirp rate γ is transmitted from the radar. Then, the demodulated echoes from target P can be expressed as

$$s(\tau, X) = \text{rect}\left(\frac{\tau - t_p}{T_p}\right) \cdot \text{rect}\left(\frac{X}{L}\right) \cdot \exp\left[j\pi\gamma(\tau - t_p)^2\right] \cdot \exp\left[-j\frac{4\pi}{\lambda}R(X; r_p, \Theta_p)\right], \quad (2)$$

where τ is the fast time, λ is the wavelength, and

$$\text{rect}\left(\frac{X}{L}\right) = \begin{cases} 1, & -\frac{L}{2} \leq X < \frac{L}{2}, \\ 0, & \text{elsewhere.} \end{cases}$$

Applying the Fourier transform (FT) with respect to the fast time, we transfer (2) into the range frequency domain, expressed as

$$S(f_r, X) = \text{rect}\left[\frac{f_r}{T_p \cdot \gamma}\right] \cdot \text{rect}\left[\frac{X}{L}\right] \cdot \exp\left[-j\frac{4\pi}{c}(f_c + f_r)R(r_p, \Theta_p; X)\right] \cdot \exp\left(-j\pi\frac{f_r^2}{\gamma}\right), \quad (3)$$

where f_r is the range frequency and f_c is the carrier frequency. Applying the matched-filtering in the range direction, the range-compressed signal is given by

$$s_{\text{MF}}(\tau, X) = \text{sinc}[B \cdot (\tau - t_p)] \cdot \text{rect}\left(\frac{X}{L}\right) \cdot \exp\left[-j4\pi\frac{R(X; r_p, \Theta_p)}{\lambda}\right], \quad (4)$$

where $\text{sinc}(x) = \sin(\pi x)/\pi x$ is the sinc function.

2.2 Azimuth impulse response function in the back-projected image

In this subsection, the principle of BP algorithm is first introduced. Our particular focus is the derivation of the azimuth impulse response function (AIRF) of the back-projected image. The obtained analytic expression of the AIRF reveals that there exists an approximate but sufficiently accurate FT relationship between the BP image and its corresponding range-compressed phase history. As we mentioned earlier, the derivation of the AIRF expression is important to form a theoretic basis for the analysis of the BP mechanism. The AIRF also paves a way to the modification of the original FFBP algorithm so that highly squinted SAR data in the presence of severe motion error can be processed. The extension of the AIRF to the cases with motion errors and the modification of the FFBP formulation are described in the next section.

The time-domain BP algorithm is implemented by a coherent integral along the range history corresponding of the target. This BP integral is performed in the range-compressed and azimuth time domain. In order to obtain an analytic expression of BP AIRF, the BP integral that renders the back-projected pixel at a polar coordinate (r_p, Θ_p) is given by

$$I(r_p, \Theta_p) = \int_{-L/2}^{L/2} s_{\text{MF}}\left(\tau = \frac{2R(r_p, \Theta_p; X)}{c}, X\right) \cdot \exp\left[j4\pi\frac{R(r_p, \Theta_p; X)}{\lambda}\right] dX. \quad (5)$$

This simple BP formulation performs a coherent integral along a specific range history corresponding to each pixel to calculate its scattering coefficient. Without any complex assumption and approximation, the BP algorithm is inherently suitable to precisely solve the range-azimuth coupling problem in SAR systems, including the highly squint mode. In a point-by-point manner, the BP can achieve the optimal focusing capability of SAR images. On the contrary, conventional Doppler-domain algorithms suffer from focus degradation due to the approximations involved in their formulations, which ultimately prevent Doppler-domain algorithms from the generation of high accuracy images. In this sense, the BP algorithm would be an effective solution to high-resolution highly squinted SAR imaging. The AIRF of sub-aperture BP image has been introduced in [31], and herein we extend it to the highly squinted case. In order to achieve an analytic expression of the AIRF in the BP image, the BP integral for a certain pixel at coordinate (r_p, Θ) is calculated as

$$I(r_p, \Theta) = \int_{-L/2}^{L/2} s_{\text{MF}}\left(\tau = \frac{2R(r_p, \Theta; X)}{c}; X\right) \cdot \exp\left[j\frac{4\pi}{\lambda}R(r_p, \Theta; X)\right] dX$$

$$\begin{aligned}
&= \int_{-L/2}^{L/2} \exp \left\{ j \frac{4\pi}{\lambda} [R(r_p, \Theta; X) - R(r_p, \Theta_p; X)] \right\} dX \\
&= \int_{-L/2}^{L/2} \exp \left[j \frac{4\pi}{\lambda} \Delta R(r_p, \Theta; X) \right] dX, \tag{6}
\end{aligned}$$

where $\Delta R(r_p, \Theta; X)$ is defined as the difference between range histories $R(r_p, \Theta; X)$ and $R(r_p, \Theta_p; X)$ whose Taylor series expansion is expressed as

$$\Delta R(r_p, \Theta; X) = R(r_p, \Theta; X) - R(r_p, \Theta_p; X) = -(\Theta - \Theta_p) \cdot X - \frac{\Theta^2 - \Theta_p^2}{2r_p} \cdot X^2 + \sigma(X^3). \tag{7}$$

If the second- and high-order terms in (7) are negligible, the BP AIRF in (6) becomes

$$I(r_p, \Theta) \approx \int_{-L/2}^{L/2} \exp \left[-j \frac{4\pi}{\lambda} (\Theta - \Theta_p) X \right] dX = L \cdot \text{sinc} \left[\frac{2L}{\lambda} (\Theta - \Theta_p) \right]. \tag{8}$$

Eq. (8) clearly shows that, in this case, the AIRF is approximately a sinc function. This result is important to derive an expression for the angular WN. Before presenting this content, we first investigate the precision aspect of the approximated AIRF below.

Given a certain aperture length L , the magnitude of the quadratic term in (7) increases as $\Delta\Theta = \Theta - \Theta_p$ deviates from zero. In general, the vast majority of the energy of AIRF is intensively concentrated within a very small region around Θ_p , and the region size corresponds to the angular resolution. Taking the angle coordinate of the point into account, the angular resolution across the beam center is given by [30]

$$\delta\Theta = \frac{\lambda}{2L}. \tag{9}$$

To analyze the effect of the quadratic term in (7) on the shape of the AIRF, the quadratic term corresponding to the neighboring region around Θ_p is rewritten as

$$\frac{(\Theta_p^2 - \Theta^2)}{2r_p} \cdot X^2 = \frac{[\Theta_p^2 - (\Theta_p + \Delta\Theta)^2]}{2r_p} \cdot X^2 \approx -\frac{\Delta\Theta \cdot \Theta_p}{r_p} \cdot X^2. \tag{10}$$

This term induces the following quadratic phase error (QPE) in (6),

$$\text{QPE} = 4\pi \frac{\Delta\Theta \cdot \Theta_p}{\lambda r_p} \cdot X^2, \tag{11}$$

whose magnitude is linearly proportional to $\Delta\Theta$. When the magnitude of QPE is sufficiently small, e.g., small than $\pi/8$, its effect on (8) is negligible. Similar to the impulse response functions of conventional SAR, the energy of the BP AIRF is highly concentrated in the several nearby pixels around grid Θ_p . As a result, the shape of AIRF is determined by its magnitude within a limited range of $[\Theta_p - \delta\Theta, \Theta_p + \delta\Theta]$. If the QPE is sufficiently small at the boundaries, its effect on AIRF is minimal. Substituting $\Delta\Theta = \delta\Theta = \lambda/(2L)$ into (11), we have $\text{QPE} = 2\pi \frac{\Theta_p}{L \cdot r_p} \cdot \left(\frac{L}{2}\right)^2$. By constraining QPE to be smaller than $\pi/8$, we obtain the condition for QPE to have negligible effects on the AIRF, i.e.,

$$\text{QPE} = 2\pi \frac{\Theta_p}{L \cdot r_p} \cdot \left(\frac{L}{2}\right)^2 \leq \frac{\pi}{8}, \tag{12}$$

or $\Theta_p L \leq r_p/4$. That is, the approximation in (8) is precise to ensure the FT pair in (8) if $\Theta_p L$ is shorter than a quarter of r_p . This constraint is generally satisfied in practice. For the sake of quantitatively understanding, consider an X-band SAR operating with a squint angle of 50° for a target with range

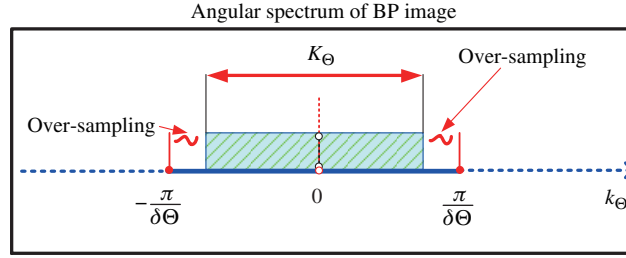


Figure 2 (Color online) Angular spectrum of BP image.

10 km and an synthetic aperture of 3.26 km. In this case, the constraint in (12) is satisfied when the azimuth resolution across the beam center is smaller than 0.1 m. Note that the above $\pi/8$ QPE constraint is a strict threshold in practice and can be relaxed without compromising the precision of the sinc approximation of the AIRF in general SAR scenarios, including a highly squint mode.

The analytic expression of the BP AIRF in (8) is very important to understand the angular spectrum characteristics of BP images. For simplicity, we only consider the image line along $r = r_p$ and rewrite (8) as $I(\Theta) = L \cdot \text{sinc}[\frac{2L}{\lambda}(\Theta - \Theta_p)]$. By applying the FT to $I(\Theta)$, we arrive at the expression of the angular WN spectrum, given by

$$I(k_\Theta) = \int I(\Theta) \cdot \exp(-jk_\Theta\Theta) d\Theta = \text{rect}\left(\frac{k_\Theta}{K_\Theta}\right) \cdot \exp(-jk_\Theta\Theta_p), \quad k_\Theta \in \left[-\frac{K_\Theta}{2}, \frac{K_\Theta}{2}\right), \quad (13)$$

where k_Θ is defined as the angular WN corresponding to Θ and $K_\Theta = \frac{4\pi}{\lambda} \cdot L$ is the angular WN width. The above expression is informative in revealing the properties of BP images. It is clear from (8) and (13) that the angular WN k_Θ and the azimuth sampling position X are bridged by the following simple relationship:

$$k_\Theta = \frac{4\pi}{\lambda}X, \quad k_\Theta \in \left[-\frac{K_\Theta}{2}, \frac{K_\Theta}{2}\right).$$

That is, in the ideal case of a straight and evenly sampled synthetic aperture, a linear relationship exists between k_Θ and X , and the spectrum center exactly corresponds to the aperture center. This relationship clearly reveals the underlying relationship between azimuth time and angular WN domains when performing BP imaging. According to (13), one can also easily derive the angular resolution as $\delta\Theta = \frac{\lambda}{2L}$, which coincides with the definitions of the angular resolution as shown in references [30]. As a result, spectrum ambiguity can be avoided through azimuth over-sampling, i.e., by setting a small width of the angular grid in the BP image, namely, $\Delta\Theta$ set to be smaller than $\delta\Theta$. In general, considerable azimuth over-sampling is necessary, leading to a significant margin in the spectrum domain. As we will describe in the next section, azimuth over-sampling is useful to avoid spectrum distortions and aliasing in the presence of severe motion errors. The angular spectrum and sampling rate requirement are demonstrated in Figure 2. It should be emphasized that over-sampling is especially crucial in FBP algorithms [28–31, 33], where the image-domain interpolation for SA image fusion does not allow any spectrum aliasing or folding. As we will show in the next section, the relationship in (13) will no longer hold when significant motion errors are present in the airborne SAR scenarios.

2.3 Fast factorized back-projection algorithm

Although the BP algorithm is flexible and precise for SAR imaging, it is generally impractical due to its prohibitive computational complexity. Inheriting the precision merits of the BP algorithm, FBP algorithms [28–30] accelerate the BP integral by dividing it into multiple SA BP integrals. The coarse images formed with the SAs are then fused to yield the high-resolution final image. Due to the fact that SA images with a coarse angular resolution are back-projected in different local polar coordinates, two-dimensional (2D) interpolation in the image domain is necessary in the fusion of the SA images. As such, the local polar coordinate (LPC), rather than rectangular coordinates, is more useful since successful interpolation requires no aliasing and folding in the corresponding angular spectrum domain [28]. Among

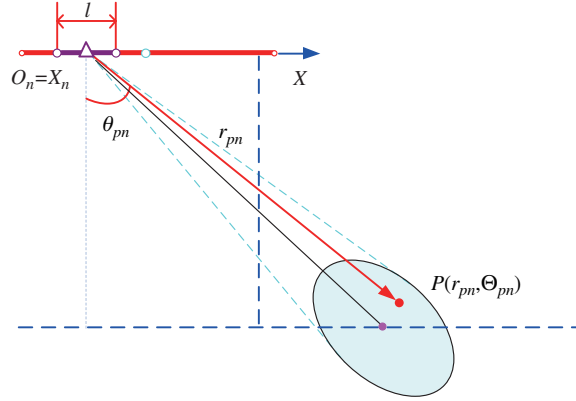


Figure 3 (Color online) Polar coordinates for SA BP imaging.

FBP algorithms, FFBP is an important representative. The basic principle behind the FFBP lies in that the grid of the coordinate can be sparsely designed without losing any information in the BP imaging of a short SA, whereas the computational load can be dramatically reduced. Assume that we split the full aperture into N SAs of an equal length of $l = L/N$. In order to achieve a high efficiency, a small SA length l should be used. In the first stage of FFBP, each SA data is back-projected onto the LPC. According to (5), for the n th SA, $n = 1, \dots, N$, the obtained coarse image I_n is computed from the BP integral as

$$I_n(r, \Theta) = \int_{-l/2}^{l/2} s_{MF} \left[\tau = \frac{2R(X; r, \Theta)}{c}, X \right] \cdot \exp \left[j \frac{4\pi}{\lambda} R(X; r, \Theta) \right] dX. \quad (14)$$

For clear understanding of the SA imaging in FFBP, we use Figure 3 to illuminate the SAR geometry of the SA LPC. In Figure 3, $X_n = (n - \frac{1}{2}) \cdot l$ denotes the center of the n th SA and is used as the LPC origin corresponding to this SA. Clearly, the AIRF and the corresponding angular WN spectrum of the SA BP image can be obtained from (8) and (13) and are expressed as

$$I_n(\Theta) = l \cdot \text{sinc} [K_{\Theta SA} (\Theta - \Theta_p)] \quad \text{and} \quad I_n(k_{\Theta}) = \text{rect} \left(\frac{k_{\Theta}}{K_{\Theta}} \right) \cdot \exp(-jk_{\Theta} \Theta_p), \quad (15)$$

where $K_{\Theta SA} = \frac{4\pi}{\lambda} \cdot l$ is the angular WN width of the SA image. Due to the short SA length, the sinc approximation of the AIRF would be much more accurate, and the given properties of the BP AIRF described in (12) and (13) remain valid. The FT relationship in (15) is very useful to derive the angular grid requirement for SA BP image. In order to avoid spectrum ambiguity, the *Nyquist* sampling criterion requires the grid of the SA image to be restricted by

$$\delta\Theta_{SA} \leq \frac{\lambda}{2l}. \quad (16)$$

In the SA fusion of FFBP, several (usually two) neighboring SA images from the previous recursion are then fused into one SA image corresponding to new LPC with a finer angular resolution. Correspondingly, the azimuth sampling rate is increased in each stage of the FFBP recursion until all SAs are fused together. For the g th FFBP recursion, we assume that there are U_g SA images corresponding to the U_g LPCs. For the n th SA image, the corresponding SA length is defined by $l^{(g)}$ and the LPC are denoted by $(r_n^{(g)}, \Theta_n^{(g)})$ with SA center X_n . For clarity, we use superscript “ g ” to express the g th FFBP recursion and subscript “ n ” to denote the n th SA. Figure 4 illustrates the FFBP recursion. Detailed principle and implementation of FFBP can be found in [30].

Regarding the BP AIRF and the spectrum expression in (15), we emphasize two important issues in FFBP implementation to clearly understand SAR imaging with FFBP. The first issue lies in the selection of back-projected coordinate for SA image. That is, Eq. (15) provides a simple but clear interpretation of the fact that the LPC is an optimal choice for SA BP image, as revealed in [30], where the angular

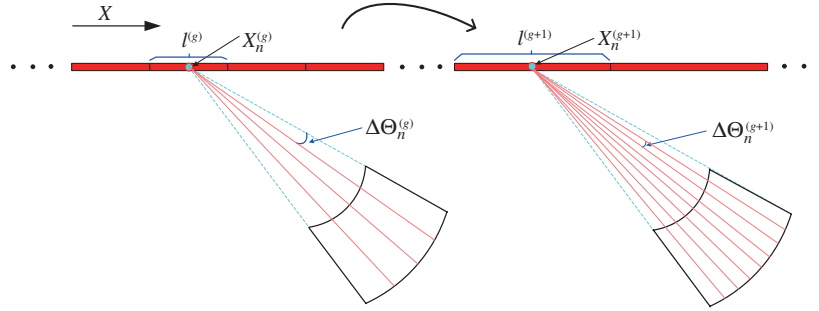


Figure 4 (Color online) Recursive SA fusion in FFBP.

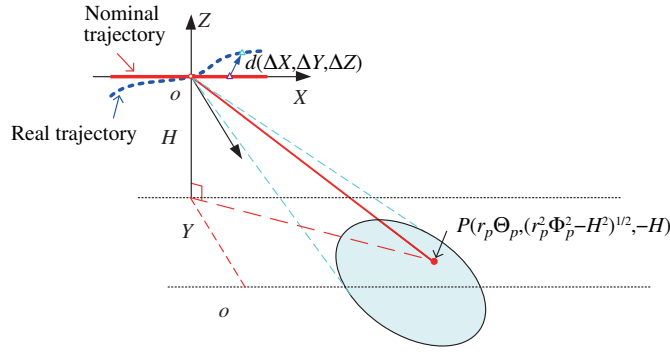


Figure 5 (Color online) Airborne SAR geometry.

grid can be set by (16) to ensure that angular spectrum aliasing is avoided in the resulting SA image. The second issue is related to the SA fusion. In general, SA fusion in the FFBP is implemented by a 2D interpolation in the image domain. A primary condition for successful interpolation is that no spectrum aliasing or folding occurs in the SA images. Actually, any interpolation kernel is deemed to fail in the presence of spectrum aliasing or folding. The optimal interpolation kernels can be used in the FFBP [34, 35] are not an exception. As a result, the FFBP algorithm usually requires a considerable angular over-sampling in practice to ensure a high performance of the interpolation.

3 Modified FFBP for the focusing of squint-mode airborne SAR

Although the FFBP algorithm can, in theory, effectively focus SAR data with an arbitrary aperture geometry, it may fail in squint-mode airborne SAR imaging, as addressed in the sequel. Based on the derivation presented in the last section, we will first introduce the spectrum aliasing effect caused by spectrum displacement because of the motion errors in the SA BP integrals involved in the FFBP algorithm. It should be emphasized that this aliasing effect is generally inevitable in airborne SAR operations, and may become significant and result in SA fusion failures in the original FFBP. If the spectrum displacement is not properly accounted for, the quality of FFBP image degrades significantly, resulting in severe false targets and resolution loss in azimuth. In this section, in order to integrating MOCO with FFBP seamlessly, a modified FFBP scheme is established to obtain high-quality imagery of squint-mode airborne SAR.

3.1 Spectrum displacement of SA BP image caused by motion errors

A three-dimensional (3D) airborne SAR data acquisition geometry is shown in Figure 5, where the solid red horizontal line along the X-axis denotes the nominal trajectory of the radar platform, and the dashed blue curve denotes its true trajectory. Denote t_m as the slow time. The ideal antenna phase center (APC) is located at $X = Vt_m$ along the X-axis at a reference height of H . The true and the nominal APC positions at slow time t_m are $[X + \Delta X(t_m), \Delta y(t_m), \Delta z(t_m)]$ and $[X, 0, 0]$, respectively,

and the corresponding instantaneous motion error vector $d = [\Delta X(t_m), \Delta y(t_m), \Delta z(t_m)]$ is defined as the displacement between the true and nominal trajectories. Consider a point target P located at Cartesian coordinate $(x_p, y_p, -H)$, where $x_p = r_p \Theta_p$, $\Phi_p = \sqrt{1 - \Theta_p^2}$, and $y_p = \sqrt{r_p^2 \Phi_p^2 - H^2}$. Taking the motion error into account, we rewrite the instantaneous range from the actual APC to the target as

$$R(X; r_p, \Theta_p) = \sqrt{(X + \Delta X - r_p \Theta_p)^2 + (\sqrt{r_p^2 \Phi_p^2 - H^2} - \Delta Y)^2 + (H + \Delta Z)^2}. \quad (17)$$

For the recorded squint-mode SAR data corrupted by the motion error, we can obtain N SA images after the first-stage FFBP procedure is accomplished for each SA. In order to investigate the influence of motion errors on SA images in FFBP, we derive the AIRF in the motion error case.

For the n th SA image with SA time interval $t_m \in [-\frac{l}{2v}, \frac{l}{2v}] + \frac{X_n}{v}$, for instance, the SA BP integral can also be expressed by (14). The difference of the range histories is expressed as

$$\Delta R(X; r_p, \Theta) = R(X; r_p, \Theta = \Theta_p + \Delta\Theta) - R(X; r_p, \Theta_p). \quad (18)$$

Substituting (17) into (18) and applying the first-order Taylor series expansion with respect to $\Delta\Theta$, we approximate (18) as

$$\Delta R(X; r_p, \Theta) \approx -X \cdot \Delta\Theta + X_F \cdot \Delta\Theta, \quad (19a)$$

where

$$X_F = -\Delta X \cdot \frac{r_p \Phi_p}{R_{p0}} + \Delta Y \cdot \frac{r_p^2 \beta_p \Theta_p}{y_p R_{p0}} \approx \left(-\Delta X + \Delta Y \cdot \frac{r_p}{y_p} \Theta_p \right) \Phi_p, \quad (19b)$$

$y_p = \sqrt{r_p^2 \Phi_p^2 - H^2}$, and $R_{p0} = \sqrt{(r_p \Theta_p - X)^2 + r_p^2 \Phi_p^2}$. In order to overcome the motion error in the FFBP imaging, the SA BP integrals are performed along the range history in (17). As a result, precise MOCO is obtained inherently without increasing the complexity of the BP procedure. By exploiting the results of (19) into (14), the AIRF can be rewritten for the n th SA image as

$$\begin{aligned} I_n(r_p, \Theta) &= \int_{-l/2}^{l/2} \exp \left[j \frac{4\pi}{\lambda} \Delta R(r_p, \Theta; X) \right] dX \\ &\approx \int_{-l/2}^{l/2} \exp \left[-j \frac{4\pi}{\lambda} X \cdot (\Theta - \Theta_p) \right] \cdot \exp \left[j \frac{4\pi}{\lambda} X_F \cdot (\Theta - \Theta_p) \right] dX. \end{aligned} \quad (20)$$

In general, the exponential term $\exp \left[j \frac{4\pi}{\lambda} X_F \cdot (\Theta - \Theta_p) \right]$ in (20) caused by the motion error is usually not negligible for airborne SAR imaging and, hereby, induces both spectrum displacement and distortion in the BP AIRF. In order to investigate the spectrum displacement, we divide X_F into a constant term X_{FC} and a time-varying term X_{FT} , i.e., $X_F = X_{FC} + X_{FT}$, where X_{FC} yields a large spectrum displacement whereas X_{FT} causes an insignificant spectrum distortion. To compensate these effects, we first focus on the spectrum displacement induced by the constant term X_{FC} , which is expressed as

$$X_{FC} = \left(-\Delta X_{cn} + \Delta Y_{cn} \cdot \frac{r_p}{y_p} \Theta_p \right) \cdot \Phi_p, \quad (21)$$

where ΔX_{cn} and ΔY_{cn} respectively represent the mean value of $\Delta X_n(t_m)$ and $\Delta Y_n(t_m)$ within the SA. For a clear explanation, Figure 6 shows the deviation from the nominal SA center to the true SA center, and the deviation vector is denoted by $\vec{o_n \hat{o}_n}(\Delta X_{cn}, \Delta Y_{cn}, \Delta Z_{cn})$. In real airborne SAR scenarios, the existence of X_{FC} will introduce a significant spectrum displacement to the SA BP image.

In addition to the angular spectrum displacement, spectrum distortion would also occur due to the presence of X_{FT} . The exponential term corresponding to the time-varying part X_{FT} in (20) causes small distortions in the AIRF, including an insignificant spectrum extension. Actually, the effects of X_{FT} on

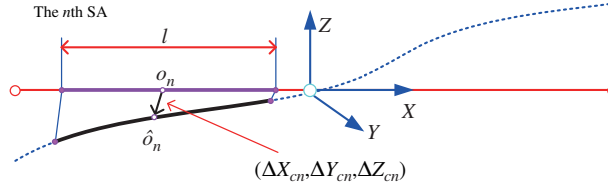


Figure 6 (Color online) Motion error geometry.

the FFBP image is negligible if a high angular over-sampling rate is used, making the resulting image to be more tolerate to such a spectrum distortion. In this case, the AIRF becomes

$$\begin{aligned} I_n(r_p, \Theta) &\approx \int_{-l/2}^{l/2} \exp\left[-j\frac{4\pi}{\lambda}X \cdot (\Theta - \Theta_p)\right] dX \cdot \exp\left[j\frac{4\pi}{\lambda}X_{FC} \cdot (\Theta - \Theta_p)\right] \\ &= l \cdot \text{sinc}\left[\frac{2l}{\lambda}(\Theta - \Theta_p)\right] \cdot \exp\left[j\frac{4\pi}{\lambda}X_{FC} \cdot (\Theta - \Theta_p)\right]. \end{aligned} \quad (22)$$

Subsequently, by applying the FT to $I_n(r_p, \Theta)$, the angular WN spectrum can be expressed as

$$\begin{aligned} I_n(r_p, k_\Theta) &= \int I_n(r_p, \Theta) \cdot \exp(-jk_\Theta\Theta) d\Theta \\ &= \text{rect}\left(\frac{k_\Theta - k_{\Theta F}}{K_{\Theta SA}}\right) \cdot \exp[-j(k_\Theta - k_{\Theta F})\Theta_p], \quad k_\Theta \in \left[-\frac{K_{\Theta SA}}{2}, \frac{K_{\Theta SA}}{2}\right], \end{aligned} \quad (23)$$

where

$$k_{\Theta F} = \frac{4\pi}{\lambda}X_{FC}. \quad (24)$$

The derivation of (23) is analogous to that of (14).

Ideally, the center of the angular WN spectrum is always located at the zero WN. When motion error is accounted in the BP SA image, however, additional spectrum displacement definitely occurs. Figure 7 illustrates the difference between the ideal and the actual MOCO angular spectra. On the other hand, the expression of spectrum shift also reveal a fact that, if the coordinate origin of the sub-aperture coordinate is set at the real SA center, the spectrum shift can be eliminated significantly. Of course, additional computation burden involves in the SA image fusion stage as we have to specifically calculating the back-projected image coordinate for each SA image. This may not suitable for the real implementation of FFBP in reality. In the following, we introduce some modification but without changing the standard FFBP procedure to effectively solve the spectrum shift problem.

In the first stage of FFBP, although the trajectory deviations are well accounted for by using the exact range history in the SA BP integral, they induce additional spectrum displacements in SA BP images. Those spectrum displacements would cause SA spectrums aliasing and folding, even when a high oversampling rate is used to achieve a sufficiently small angular grid, leading to failures of the interpolation-based SA fusion in the following FFBP stages. Notably, as we desire a high-efficiency FFBP formation, the SA length should be kept very short, e.g., 16 pulses, in real-data processing. The spectrum width boundary $\frac{\pi}{\delta\Theta}$ in Figure 6 is usually very small in the first stage of FFBP. On the other hand, the track deviations, ΔX_{cn} and ΔY_{cn} , may be in the order of several meters. They yield a substantial value of $k_{\Theta F}$ and, in turn, cause the aliasing and folding effects as shown in Figure 6(b). In order to ensure a successful SA fusion in FFBP image formation of squinted airborne SAR, the spectrum displacement should be handled appropriately.

3.2 Modified FFBP algorithm

The above discussion of spectrum displacement in FFBP motivates us to develop a modified FFBP framework for high-resolution squinted airborne SAR imaging. In the first stage, conventional SA BP integrals are performed to generate a series of SA images with a coarse angular resolution. The key modification

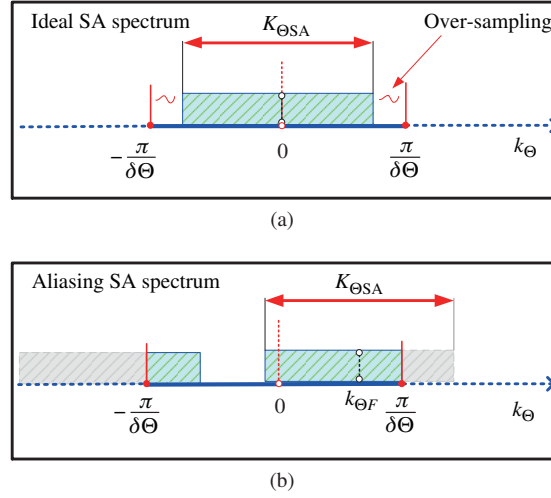


Figure 7 (Color online) SA BP image spectrums. (a) Ideal SA spectrum; (b) aliasing SA spectrum.

lies in that, in the recursion of SA fusion, neighboring SA images are first multiplied by an exponential function to remove the angular spectrum displacement before fusing the images through the interpolation. When the interpolated component is obtained, the corresponding phase term is subsequently corrected. The proposed algorithm is termed as the modified FFBP (MFFBP), which is described in the following major steps:

1. Similar to the first stage of the original FFBP, the full aperture is split into N SAs, and SA BP integrals are performed by combining the auxiliary position measurements from POS. In this step, we can also easily calculate the spectrum displacements for each SA image according to the position measurements described in (21) and (24). Denote $k_{\Theta F_n}$ as the amount of the spectrum displacement of the n th SA image. We emphasize that the range dependence of variable $k_{\Theta F_n}$ is usually negligible in typical airborne SAR scenarios. That implies that $k_{\Theta F_n}$ can be evaluated at the range center for all range blocks of the image, leading to significant reduction of the computation complexity.

2. Before we perform SA fusion with the angular interpolation, the SA images are multiplied by an exponential function to remove the angular spectrum displacement. That is,

$$\hat{I}_n(r, \Theta) = I_n(r, \Theta) \cdot \exp(jk_{\Theta F_n} \cdot \Theta), \quad (25)$$

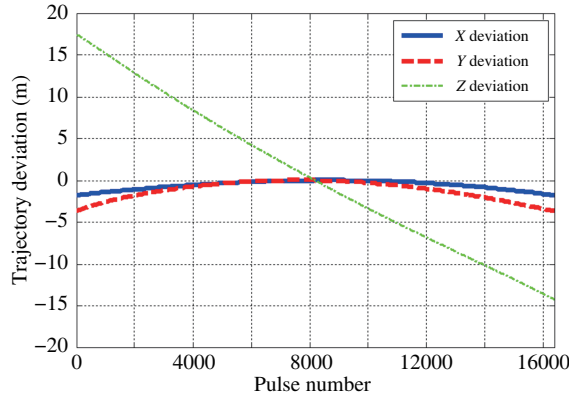
where $I_n(r, \Theta)$ is the n th SA image and $\hat{I}_n(r, \Theta)$ denotes the one after correcting the spectrum displacement. Then, angular interpolation is performed on $\hat{I}_n(r, \Theta)$ rather than $I_n(r, \Theta)$ to mitigate the effects of the spectrum aliasing on SA fusion. The corresponding phase term should be compensated back in each angular bin after the image at that bin is interpolated. For example, we obtain an arbitrary angular component at angular coordinate $\Theta = \Theta_a$ as $\hat{I}_n(r, \Theta_a)$. The phase term in (25) on that angular bin should be removed before fusing it into a high-resolution SA image for the next recursion, i.e.,

$$I_n(r, \Theta_a) = \hat{I}_n(r, \Theta_a) \cdot \exp(-jk_{\Theta F_n} \cdot \Theta_a). \quad (26)$$

3. We perform SA fusion recursively like the original FFBP, but the important distinction between them is that the proposed method accounts the spectrum displacements in each stage according to the real sub-aperture measured by auxiliary position systems mounted in the platform. The phase correction in (25) and (26) is performed for each SA in all FFBP recursions until the full-resolution image is obtained in the polar coordinate. In this scheme, motion compensation can be embedded in FFBP seamlessly. It should be emphasized that, additional computation required for the spectrum displacement correction is only a small fraction of the entire computational load of FFBP. As a result, the proposed MFFBP maintains the same high efficiency as the original FFBP when dealing with high-resolution highly squinted airborne SAR data.

Table 1 Main system parameters

Wave band	X-band
Pulse duration	5
Pulse bandwidth	600 MHz
Platform velocity	132 m/s
Pulse repetition frequency (PRF)	2000 Hz
Squint angle	40.2°
Center line of scene	15.2 km

**Figure 8** (Color online) Trajectory deviations measured by a position system.

4 Experimental results

To validate the effectiveness of the proposed approach, a real data example is presented in this section. Real airborne data collected from an experimental X-band SAR with the squinted spotlight mode is used to verify the performance of the proposed MFFBP and compare it with that of the original FFBP formation.

The main parameters of the SAR system are tabulated in Table 1. In the experiment, the synthetic aperture time was 8.2 s acquiring 16384 pulses with each pulse containing 16384 range bins. The 3D motion errors in the Cartesian coordinate are plotted in Figure 8. Those measurements are recorded by a position system mounted on the radar, and are utilized to compute the instantaneous range in the following FFBP formations. Severe motion errors are observed in Figure 8. Especially, the deviation in the Z direction is up to 30 m, whereas those in the Y and X directions are as high as several meters. Such large motion deviations are challenging to current Doppler-domain MOCO algorithms. As we will show, however, such situation can be properly processed by the proposed MFFBP algorithm.

We produce high-resolution and wide-swath SAR imagery by both the original FFBP and the proposed MFFBP with the spectrum displacement correction. In the first stage, both algorithms generate identical coarse-resolution SA images from a data set with a 25% oversampling ratio, where the entire synthetic aperture is equally divided into 512 SAs, each of 32 pulses. Note that certain oversampling ratio is necessary to ensure the performance of the FFBP algorithms at an expense of increased computational burden. It can also alleviate the influence of spectrum displacement in a certain extent when the original FFBP is used to focus airborne SAR data in the presence of insignificant motion errors. Without loss of generality, we always combine two neighboring SA images into one image in each FFBP recursion. As a result, the FFBP formations require 9 recursions to fuse the coarse SA images into a full-resolution image in the polar coordinate. It should also be emphasized that the spectrum displacement affects all interpolators, including the novel interpolation kernels developed in [34]. For the sake of simplicity and clarity, herein, the nearest neighbor interpolation with the 8-point FFT is utilized in both range and angular directions within the SA fusion stages. While the nearest neighbor interpolation is not the most efficient one for FFBP, it is very reliable to provide a high precision in this experiment. The generated

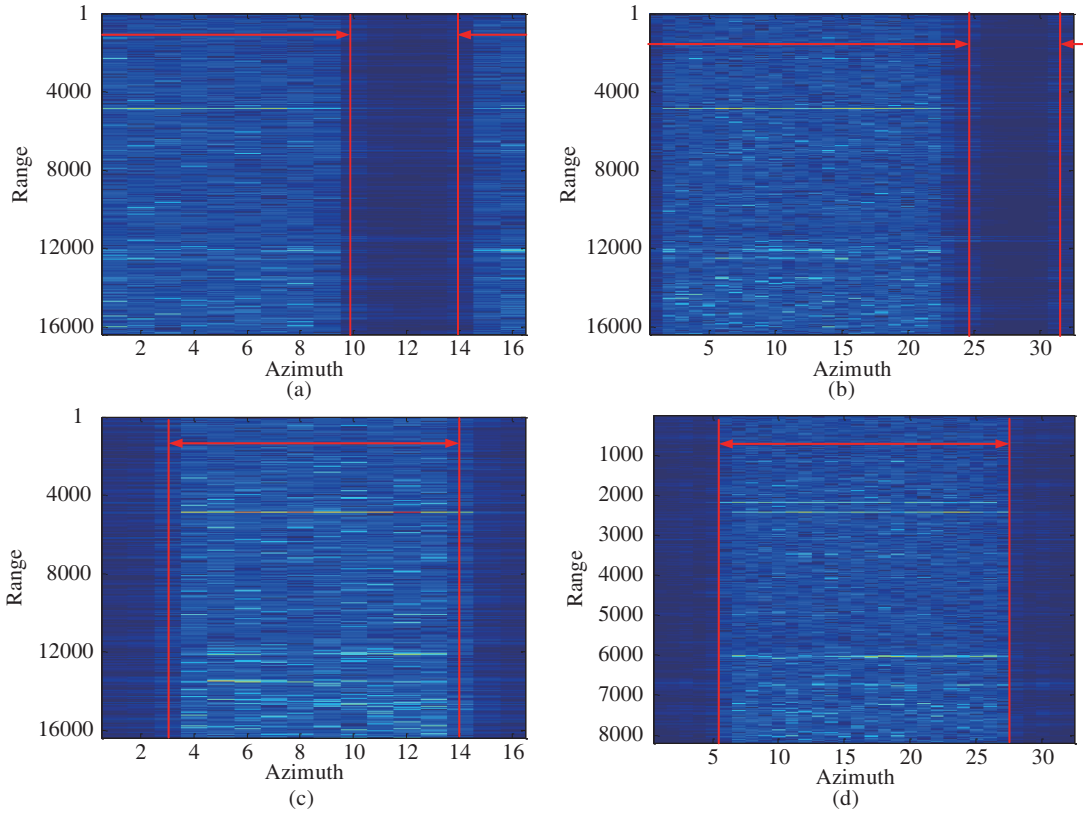


Figure 9 (Color online) WN spectra before and after shift removal in the first FFBP stage. (a) WN spectrum of the first SA image; (b) WN spectrum of the 256th SA image; (c) WN spectrum after shift removal of the first SA image; (d) WN spectrum after shift removal of the 256th SA image.

polar coordinate image is about $3 \text{ km} \times 2.4 \text{ km}$ in the range and cross-range directions with a nominal range and cross-range resolution of approximate $0.3 \text{ m} \times 0.3 \text{ m}$.

At first, we present the angular WN spectrum of the first-stage SA images of FFBP to show the spectrum displacement phenomenon. As there are 1024 SA images, we only show in Figures 9 (a) and (b) the typical WN spectra of the first and the 256th SA images by applying the Fourier transform to them. Notably, the spectra are folded even oversampling is adapted in the FFBP formation. These folding effects will surely result failures in the interpolation of the following SA fusion procedure. According to the motion deviations illustrated in Figure 7, we can also interpret the phenomenon that spectrum aliasing and folding more possibly occurs in the first and last SA images because the corresponding deviations in the first and the last synthetic apertures are more severe than those in the other apertures. Figures 9 (c) and (d) show the results after applying (26) to remove the spectrum shifts within each SA image. Clearly, the spectrum folding is removed in an optimal manner. As a result, the negative effects on the SA fusion can be eliminated.

The full-scene images obtained from the original FFBP and the MFFBP are respectively presented in Figures 10 (a) and (b). While the same motion measurements are used, the modified and the original FFBP algorithms provide distinct results. Without accounting for the spectrum shifts in SA images, the original FFBP image has a number of false targets due to the discontinuity in the angular spectrum of the fused image. In the same time, the azimuth resolution is also decreased. In contrary, the modified FFBP algorithm provides significantly improved image which achieves ideal focusing without any false targets yielded. It is clear from Figure 10(a) that the MFFBP successfully generates an image with higher contrast and clearness, and various types of targets, such as bridges, trees, and farmlands, are shown clearly.

To provide a more clear comparison between the modified and the original FFBP algorithms, the magnified sub-scenes ACE, marked in Figure 10(a), are respectively shown in Figures 11 (a)–(e). In each

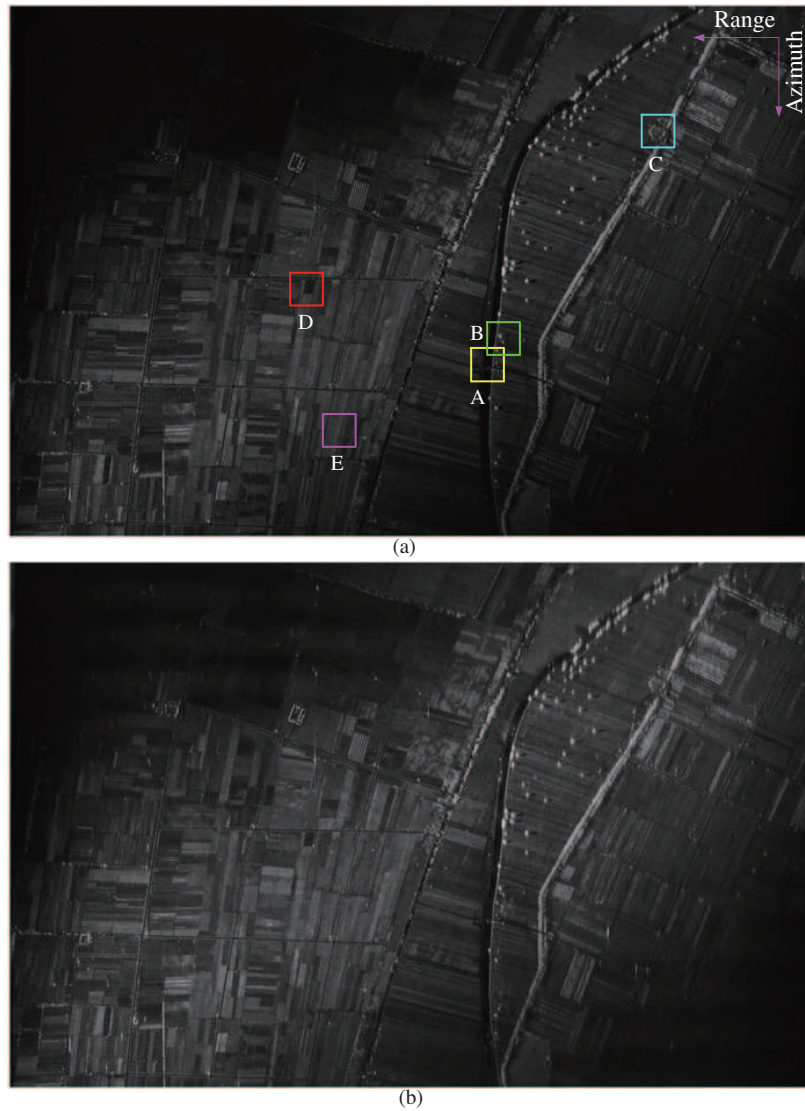


Figure 10 (Color online) Images with the modified and the original FFBP formations. (a) MFFBP image; (b) original FFBP image.

pair of sub-scene images compared in Figure 11, the right image is obtained using the original FFBP, whereas the left one is obtained by the modified FFBP approach. We note in Figure 11 that all sub-scene images generated by the proposed approach are well focused. In these figures, different types of targets are concentrated and the farmland texture is distinctive. On the other hand, since the spectrum displacement problem is not accounted for in the original FFBP formation, it yields serious false targets, such as the strong points in the center of sub-scenes D and E. Those false targets are resulted from the discontinuities in the angular spectrum of the full scene image. Such false targets are not observed in the results processed by the proposed technique that achieves a high focusing quality.

To analyze the azimuth resolution loss of the original FFBP in dealing with this data, we also give the azimuth response of two point-like scatterers in Figure 12. The two scatterers are circled in Figure 11(a), and interpolation is applied in rendering Figure 12 for the clarity of comparison. The response of an idea point-like target obtained by both the proposal and original FFBP approaches approximately represents their respective azimuth resolutions. As expected, the main-lobes of the responses obtained by MFFBP are narrower than those by the original one and the peak values are higher, indicating a higher azimuth resolution being achieved. In Figure 12(b), the 3 dB main-lobe width of the responses obtained from the proposed method is 0.33 m, which is very close to the ideal value. However, the main-lobe width of

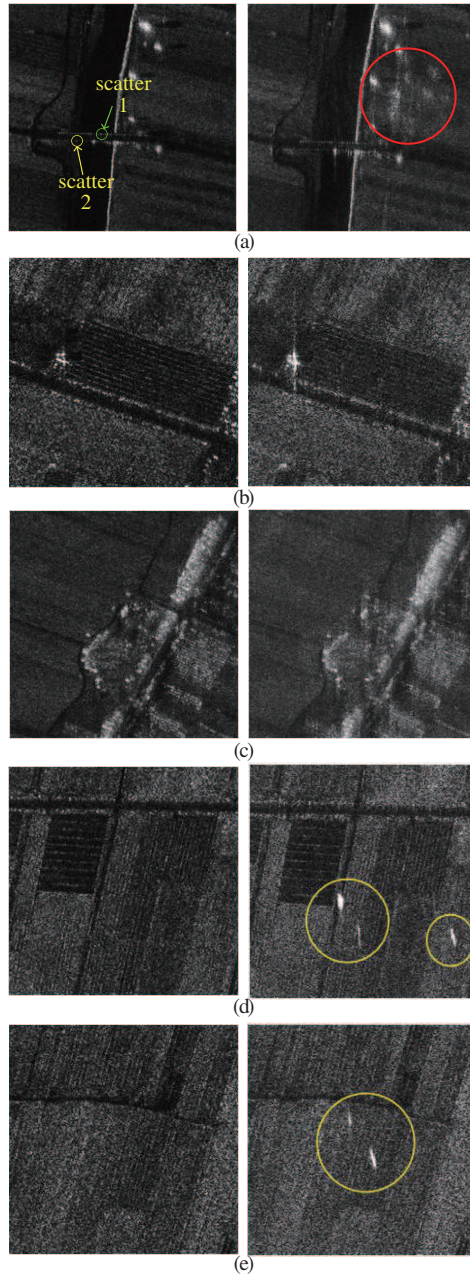


Figure 11 (Color online) Comparisons of sub-images from modified and original FFBP. (a) Sub-image of A; (b) sub-image of B; (c) sub-image of C; (d) sub-image of D; (e) sub-image of E.

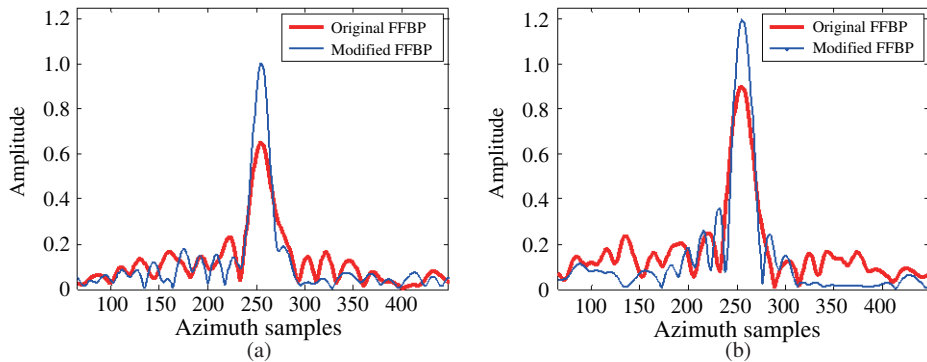


Figure 12 (Color online) Azimuth response of two point-like scatterers obtained using the modified and the original FFBP algorithms. (a) Results of scatterer 1; (b) results of scatterer 2.

the azimuth response obtained from the original FFBP is approximately 0.472 m, implying a noticeable resolution loss. The low peak values in the original FFBP image responses also imply the in effective coherent integral in the angular direction. As a result, inevitable losses of radiometric resolution occur. All the above results evidently verify the effectiveness of the proposed MFFBP method in focusing the squinted airborne SAR data.

5 Conclusion

Focusing highly squinted airborne SAR data is a challenging task for conventional Doppler-domain imaging algorithms due to the difficulties of the severe range-azimuth coupling effects as well as the precise motion compensation. In this paper, we investigated the application of fast factorization back-projection (FFBP) to solve those difficulties. We gave the analytic expression of the angular impulse response function of a highly squinted SAR BP image, which provides a new way to interpret the application of BP and FFBP. Along with the extension of AIRF by concerning severe motion errors, the relation between the spectrum displacement and trajectory deviations is revealed. And crucial modification is introduced into FFBP to successfully mitigate the motion error-induced wavenumber spectrum displacement within the sub-aperture (SA) fusion. Real data results are presented to demonstrate the spectrum displacement and verify the effectiveness of MFFBP for squinted airborne SAR imaging. The major limitation of MFFBP in real airborne SAR application is the dependence on high-precision trajectory measurements. Highly accurate real-time trajectory information would be difficult to obtain without mounting a high-quality navigation and position system. Effective combination of MFFBP and novel autofocus techniques, like map-drift algorithm [35, 36], phase gradient autofocus algorithm [37], minimum entropy algorithm [38], is worthy of deep investigation in the future work.

Acknowledgements This work was supported by National Natural Science Foundation of China (Grant Nos. 61301280, 61301293). The authors would like to thank the anonymous reviewers for their valuable comments to improve the paper quality.

Conflict of interest The authors declare that they have no conflict of interest.

References

- 1 Cumming I G, Wong F H. *Digital Processing of Synthetic Aperture Radar Data: Algorithms and Implementation*. Norwood: Artech House, 2005
- 2 Soumekh M. *Synthetic Aperture Radar Signal Processing with MATLAB Algorithms*. New York: John Wiley, 1999
- 3 Smith A M. A new approach to range-Doppler SAR processing. *Int J Remote Sens*, 1991, 12: 235–251
- 4 Raney R K, Runge H, Bamler R, et al. Precision SAR processing using chirp scaling. *IEEE Trans Geosci Remot Sens*, 1994, 32: 786–799
- 5 Moreira A, Huang Y H. Airborne SAR processing of highly squinted data using a chirp scaling approach with integrated motion compensation. *IEEE Trans Geosci Remot Sens*, 1994, 32: 1029–1040
- 6 Davidson G W, Cumming I G, Ito M R. A chirp scaling approach for processing squint mode SAR data. *IEEE Trans Aerosp Electron Syst*, 1996, 32: 121–133
- 7 Wong F H, Yeo T S. New applications of the nonlinear chirp scaling in SAR data processing. *IEEE Trans Geosci Remot Sens*, 2001, 39: 946–953
- 8 An D X, Huang X T, Jin T, et al. Extended nonlinear chirp scaling algorithm for high-resolution highly squint SAR data focusing. *IEEE Trans Geosci Remot Sens*, 2012, 50: 3595–3609
- 9 Sun G C, Xing M D, Liu Y, et al. Extended NCS based on method of series reversion for imaging of highly squinted SAR. *IEEE Geosci Remote Sens Lett*, 2011, 8: 446–450
- 10 Zhang S X, Xing M D, Xia X G, et al. Focus improvement of high-squint SAR based on azimuth dependence of quadratic range cell migration correction. *IEEE Geosci Remote Sens Lett*, 2013, 10: 150–154
- 11 Cafforio C, Prati C, Rocca F. SAR data focusing using seismic migration techniques. *IEEE Trans Aerosp Electron Syst*, 1991, 27: 194–207
- 12 Bamler R. A comparison of range-Doppler and wavenumber domain SAR focusing algorithms. *IEEE Trans Geosci Remot Sens*, 1992, 30: 706–713
- 13 Cumming G, Neo Y L, Wong F H. Interpretations of the Omega-k algorithm and comparisons with other algorithms. In: *Proceedings of IEEE International Geoscience and Remote Sensing Symposium, Toulouse, 2003*: 1455–1458

- 14 Reigber A, Alivizatos E, Potsis A, et al. Extended wavenumber-domain synthetic aperture radar focusing with integrated motion compensation. *IEE Proc-Radar Sonar Navig*, 2006, 153: 301–310
- 15 Fornaro G, Franceschetti G, Perna S. On center-beam approximation in SAR motion compensation. *IEEE Geosci Remote Sens Lett*, 2006, 3: 276–280
- 16 de Macedo K A C, Scheiber R. Precise topography- and aperture-dependent motion compensation for airborne SAR. *IEEE Geosci Remote Sens Lett*, 2005, 2: 172–176
- 17 Prats P, Reigber A, Mallorqui J J. Topography-dependent motion compensation repeat-pass interferometric SAR systems. *IEEE Geosci Remote Sens Lett*, 2005, 2: 206–210
- 18 Li Y L, Liang X D, Ding C B, et al. Improvements to the frequency division-based subaperture algorithm for motion compensation in wide-beam SAR. *IEEE Geosci Remote Sens Lett*, 2013, 10: 1219–1223
- 19 Ding Z G, Liu L S, Zeng T, et al. Improved motion compensation approach for squint airborne SAR. *IEEE Trans Geosci Remote Sens*, 2013, 51: 4378–4387
- 20 Fornaro G, Franceschetti G, Perna S. Motion compensation of squinted airborne SAR raw data: role of processing geometry. In: *Proceedings of IEEE International Geoscience and Remote Sensing Symposium, Anchorage, 2004*: 1518–1521
- 21 Zhang L, Sheng J L, Xing M D, et al. Wavenumber-domain autofocus for highly squinted UAV SAR imagery. *IEEE Sens J*, 2012, 50: 1574–1588
- 22 Yang L, Xing M D, Wang Y, et al. Compensation for the NsRCM and phase error after polar format resampling for airborne spotlight SAR raw data of high resolution. *IEEE Geosci Remote Sens Lett*, 2013, 10: 165–169
- 23 Zeng T, Li Y H, Ding Z G, et al. Subaperture approach based on azimuth-dependent range cell migration correction and azimuth focusing parameter equalization for maneuvering high-squint-mode SAR. *IEEE Trans Geosci Remote Sens*, 2015, 53: 6718–6734
- 24 Jakowatz C V, Wahl D E, Yocky D A. Beamforming as a foundation for spotlight-mode SAR image formation by backprojection. In: *Proceedings of SPIE—Algorithms for Synthetic Aperture Radar Imagery XV, Orlando, 2008*. 6970: 69700Q
- 25 Li Y H, Song Q, Jin T, et al. Arbitrary synthetic aperture motion compensation based on fast back projection. In: *Proceedings of 2010 European Radar Conference (EuRAD), Paris, 2010*. 487–490
- 26 Frey O, Magnard C, Rüegg M, et al. Focusing of airborne synthetic aperture radar data from highly nonlinear flight tracks. *IEEE Trans Geosci Remote Sens*, 2009, 47: 1844–1858
- 27 Vu V T, Sjogren T K, Petersson M I. A comparison between fast factorized backprojection and frequency-domain algorithms in UWB low frequency SAR. In: *Proceedings of IEEE International Geoscience and Remote Sensing Symposium, Boston, 2008*. 1293–1296
- 28 Yegulalp A F. Fast backprojection algorithm for synthetic aperture radar. In: *Proceedings of IEEE Radar Conference, Waltham, 1999*. 60–65
- 29 Wahl D E, Yocky D A, Jakowatz C V. An implementation of a fast backprojection image formation algorithm for spotlight-mode SAR. In: *Proceedings of SPIE—Algorithms for Synthetic Aperture Radar Imagery XV, Orlando, 2008*. 6970: 69700H
- 30 Ulander L M H, Hellsten H, Stenstrom G. Synthetic aperture radar processing using fast factorized back-projection. *IEEE Trans Aerosp Electron Syst*, 2003, 39: 760–776
- 31 Zhang L, Li H L, Qiao Z J, et al. A fast BP algorithm with wavenumber spectrum fusion for high resolution spotlight SAR imagery. *IEEE Geosci Remote Sens Lett*, 2014, 11: 1460–1464
- 32 Carrara W G, Goodman R S, Majewski R M. *Spotlight Synthetic Aperture Radar: Signal Processing Algorithm*. Boston: Artech House, 1995. 245–254
- 33 Marcelo A, Pau P, Rolf S. Applications of time-domain back-projection SAR processing in the airborne case. In: *Proceedings of the 7th European Conference on Synthetic Aperture Radar (EUSAR), Friedrichshafen, 2008*. 1–4
- 34 Frolind P-O, Ulander L M H. Evaluation of angular interpolation kernels in fast back-projection SAR processing. *IEE Proc-Radar Sonar Navig*, 2006, 15: 201–211
- 35 Zhang L, Li H L, Qiao Z J, et al. Integrating autofocus techniques with fast factorized back-projection algorithm for high-resolution spotlight SAR imagery. *IEEE Geosci Remote Sens Lett*, 2013, 10: 1394–1398
- 36 Cantalloube H M J, Nahum C E. Multiscale local map-drift-driven multilateration SAR autofocus using fast polar format image synthesis. *IEEE Trans Geosci Remote Sens*, 2011, 49: 3730–3736
- 37 Fan B K, Ding Z G, Guo W B, et al. An improved motion compensation method for high resolution UAV SAR imaging. *Sci China Inf Sci*, 2014, 57: 122301
- 38 Kragh T J, Kharbouch A A. Monotonic iterative algorithm for minimum-entropy autofocus. In: *Proceedings of IEEE International Conference on Image Processing, Atlanta, 2006*. 645–648